PNAS
www.pnas.org

Supplementary Information for

Intrinsic electronic conductivity of individual atomically-resolved amyloid crystals reveals micrometer-long hole hopping via tyrosines

Catharine Shipps[a,b], H. Ray Kelly[c], Peter J. Dahl[a,b], Sophia M. Yi[a,b], Dennis Vu[a,b], David Boyer[d,e,f,g,h],Calina Glynn[e,g,h], Michael R. Sawaya[d,e,f,g,h], David Eisenberg[d,e], Victor S. Batista[c], and Nikhil S. Malvankar[a,b,1]

[a]Department of Molecular Biochemistry and Biophysics, Yale University, New Haven, CT 06510; [b]Microbial Sciences Institute, Yale University, New Haven, CT06516; [c]Department of Chemistry, Yale University, New Haven, CT 06511; [d]HHMI, University of California, Los Angeles, CA 90095; [e]Department of Chemistry and Biochemistry, University of California, Los Angeles, CA 90095; [f]Department of Biological Chemistry, University of California, Los Angeles, CA 90095;[g]Molecular Biology Institute, University of California, Los Angeles, CA 90095; and [h]University of California, Los Angeles–Department of Energy Institute for Genomics and Proteomics, University of California, Los Angeles, CA 90095

* Corresponding author: Nikhil S. Malvankar. **Email:** nikhil.malvankar@yale.edu

This PDF file includes:

Supplementary Methods

Structure Determination of X4 Crystal: Peptide sequence - KVQIINKKL

Micro-ED Data Collection and Processing. Crystal solution was applied to a glow discharged Quantifoil R1/4 cryo-EM grid, and plunge frozen using a Vitrobot Mark 4. Micro-ED data was collected in a manner similar to previous studies(1). Briefly, plunge-frozen grids were transferred to an FEI Technai F20 electron microscope operating at 200 kV and diffraction data were collected using a TVIPS F416 CMOS camera with a sensor size of 4,096 x 4,096 pixels, each 15.6 x 15.6 µm. Diffraction data were indexed using DENZO, and SCALEPACK was used for merging and scaling together data sets from different crystals(2). 7 diffraction movies were merged using SCALEPACK to produce the final data set.

Molecular replacement was performed in PHENIX using a search model of KVQIINKKL derived from previously reported peptide structure KVQIINKKLD (PDB: 5V5B)(3). A combination of REFMAC, Phenix, and Buster refinement programs were used with electron scattering factors to refine the atomic coordinates(4-6).

Impedance Spectroscopy (IS). IS was performed at ambient room temperature and humidity. For all experiments, humidity was continuously monitored and maintained at less than 50%. The probe station connections and sample prep were identical to those for two-probe measurements. The two probe needle cables were connected to working and sense and counter and reference electrodes respectfully on a Gamry Interface1000. An AC voltage of amplitude 100 mV was applied in Potentiostatic mode sweeping from 100,000 to 0.2 Hz. Equivalent circuit modeling was performed with Echem Analyst Software, and all data was fit to a resistor and constant phase element in parallel.

Nanoelectrode Design and Fabrication. Independently addressable nanoelectrodes made of gold separated by a 300-nm non-conductive gap were designed using electron beam lithography as described previously (7). Briefly, silicon wafers with 300 nm thermally grown oxide were used as substrates. The electrodes were designed in Layout Editor and first patterned by electron-beam nano-lithography on a photoresist layer. The wafer was then developed in a solution of cooled isopropyl alcohol to remove the resist layer where the pattern was printed. A 30-nm-thick gold film on top of a 5-nm-thick titanium adhesion layer was evaporated on the wafer using an electron-beam evaporator (Denton Infinity 22). The photoresist was removed with N-Methyl-2pyrrolidone by incubating for 15-20 min at 80°C until the lift-off was complete. The device was then rinsed with acetone, methanol, and isopropanol and dried with nitrogen, resulting in gold nanoelectrodes with a 300-nm gap. All device fabrication was performed in a class 1000 cleanroom to avoid contamination. In addition to electron beam lithography, nanoimprinting was used to fabricate electrodes with 50 nm non-conducting gaps for measurements of conductance vs length for the X1 microcrystal as described previously (8). Electrode design parameters were used along with microcrystal dimension determined by Atomic Force Microscopy to calculate conductivity(9).

Density Functional Theory Calculations. All calculations were performed using the B3LYP functional(10, 11) and Grimme's D3 dispersion correction with Becke-Johnson damping(12) as implemented in Gaussian 16, Revision A.03(12, 13). For all calculations, the LANL2DZ basis set with effective core potential(13-15) was used for Zn and the 6-31G(d,p) basis set(16-18) was used for all other atoms. Solvation effects were included using a polarizable continuum model (PCM)(19). Gaussview, Version 6 was used to visualize molecular structures(20).

Four model systems (Supplementary Table 3) were constructed from the Zn^{2+}NNQQNY crystal structure (PDB 52KE(21)) to separately investigate the effect of Zn^{2+} and tyrosine stacking on the tyrosine pK_a and oxidation potential. To correctly model the Zn^{2+} coordination from the periodic crystal, the NNQQNY chains were split into NNQ and QNY chains (Supplementary Fig. 2). For models without Zn^{2+}, only the QNY chains were included. To determine the effect of tyrosine stacking, both one- and two-layer models were considered. For all optimizations, the position of Zn^{2+}, acetate C, and protein backbone atoms were kept fixed to maintain the overall structure from the microcrystal. All optimizations were performed with the default convergence criteria (maximum force of 0.00045 a.u., R.M.S. force of 0.0003 a.u., maximum displacement of 0.0018 a.u., R.M.S. displacement of 0.0012 a.u.). Redox potentials were computed by referring the absolute redox potentials obtained from the change in Gibbs free energy to the absolute

potential of the standard hydrogen electrode (+4.44 V)(22). Calculations on all model systems were performed with a water PCM implicit solvent.

Relaxed potential energy scans were performed for the two-layer model containing Zn^{2+} (Model A), in which the system was optimized at each point with the tyrosine OH bond length kept fixed. Optimizations of the two-layer model and corresponding potential energy scans were additionally calculated with PCMs for diethylether (ε = 4.24) and propanonitrile (ε = 29.3) to mimic the dielectric environments inside and at the surface of a protein respectively(23, 24).

Tyrosine pK_a values were computed using a calibration curve method as described by Matsui et al. for calculations of sidechain pK_a values in large proteins(25). The changes in free energy after deprotonation were computed for each model and compared to those for a series of phenol molecules with known pK_a values (Fig. S4, Supplementary Table 2). This method allows for the accurate calculation of the pKa of tyrosine in the amyloid chains (Supplementary Table 3) by enabling the cancellation of systematic errors in phenol pKa calculations while removing the need to rely on a value for the solvation free energy of a proton.

Molecular Dynamics Simulations. Using the crystallographic symmetry, models were built to emulate the crystalline environment, each containing a total of 70 peptides. Both models were solvated with a TIP3P water model in a rectangular box with approximate dimensions of 90 x 24 x 90 Å. The y-dimension of the water box was set to be exactly the length of the y-dimension of the microcrystal such that periodic boundary conditions would extend the stacking of the peptides infinitely. Counterions did not need to be added as the net charge of the system was neutral.

Each MD step was implemented with NAMD (26) using the CHARMM36(27) forcefield and periodic boundary conditions. The X1 system was built with a modified N-terminus to accommodate its coordination to the Zn^{2+} ion. Specifically, the third hydrogen of the NTER patch was removed and the partial charges of the nitrogen and remaining hydrogens were adjusted to match the amine of asparagine, making the new N-terminus net neutral. Except for the top peptide layer, Zn^{2+} ions were coordinated with two acetate ions and the C-terminus of the adjacent peptide. To our knowledge, there are no published parameters for Zn^{2+} coordination between these moieties. As an approximation of the coordination sphere, we introduced harmonic restraints using the NAMD extraBonds functionality. Bond lengths of 2.089 Å and 2.009 Å(28) and a force constant of 270.2 kcal/mol/$Å^2$ were introduced for the Zn^{2+}– O and Zn^{2+} – N bonds, respectively. For the top peptide layer, Zn^{2+} ions were missing a coordinating acetate. However, since each MD step was implemented with periodic boundary conditions according to the crystallographic symmetry along the z-axis, the lower acetate coordinating the Zn^{2+} ion in the bottom peptide layer would be in the position of the missing acetate, although in the next periodic image.

Relaxation and sampling of each system was performed in four steps. First, we ran a steepest descent energy minimization. We then ran a 2.5 ps fixed protein simulation to randomize the water box. Next, we equilibrated each system to the desired temperature under NVT conditions for 3.5 ns with collective variables applying harmonic restraints with a force constant of 0.5 kcal/mol to the amino acid sidechains and a force constant of 2.0 kcal/mol to the protein backbone, Zn^{2+} ions, and acetate molecules. We ran nine independent temperature equilibrations at 220 K, 230 K, 240 K, 250 K, 260 K, 270 K, 280 K, 290 K, and 300 K. The X2 system was only equilibrated at 300 K. Finally, we ran an MD production simulation under NPT conditions for 90 ns. All simulations were run with 1 fs timesteps, and frames were written to the trajectory file every 2.5 ps.

Distance analysis was performed in VMD(29) with a custom Tcl script. The analysis was performed on selected peptides from snapshots selected over the whole trajectory spaced 125 ps apart. Peptides were selected such that our dataset had representation from peptides at the edge of the system (exposed to bulk water) and peptides in the middle of the crystal (exposed to confined water channel). In total we chose 6 peptides for analysis. The edge-to-edge distance between tyrosine residues was defined as the minimum distance between carbon atoms in the aromatic ring. Hydrogen bonding frequency between the tyrosine hydroxyl and glutamine carbonyl was computed using the VMD HBonds plugin(29). The hydrogen bonding frequency was computed for each of the six selected peptides separately, and then averaged.

Supplementary Figures

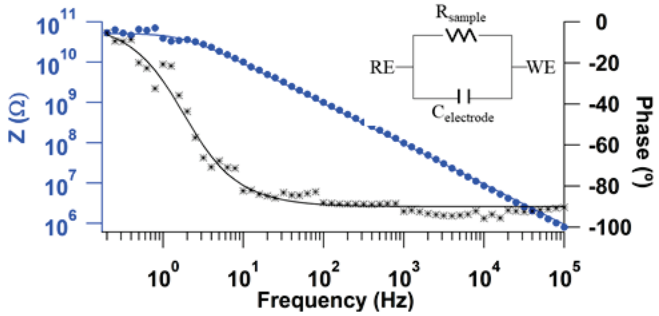

Supplementary Fig. 1 Impedance spectroscopy confirms purely electronic conductivity in amyloids. AC impedance spectroscopy (IS) on X1 single crystals. (Inset) The circuit diagram used to fit to the data. The fits for a circuit with a true capacitor were compared to those modeled with a constant phase element and no significant differences were seen.

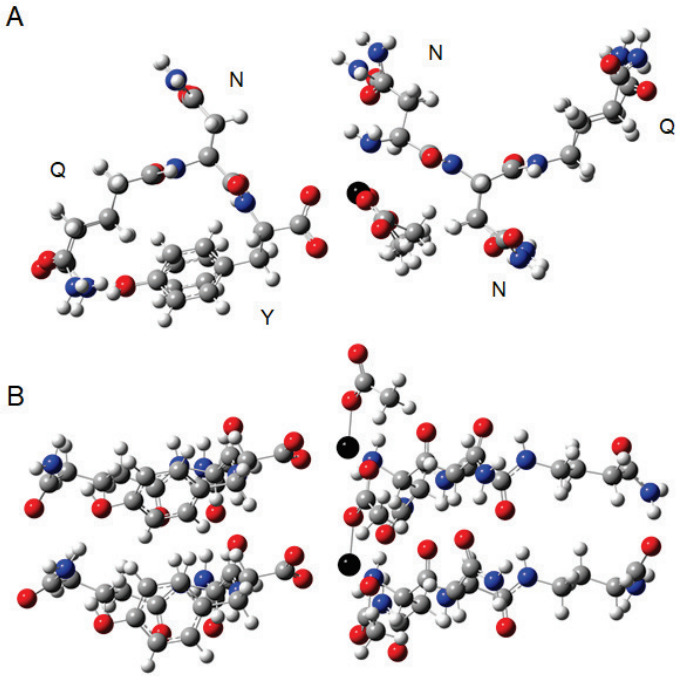

Supplementary Fig. 2. **A**, Top and **B**, side view of optimized structure of Model System A in a water PCM. This model system was used for potential energy scan calculations. Chemical elements are represented by different colors as grey: carbon, blue: nitrogen, red: oxygen, white: hydrogen, black: zinc.

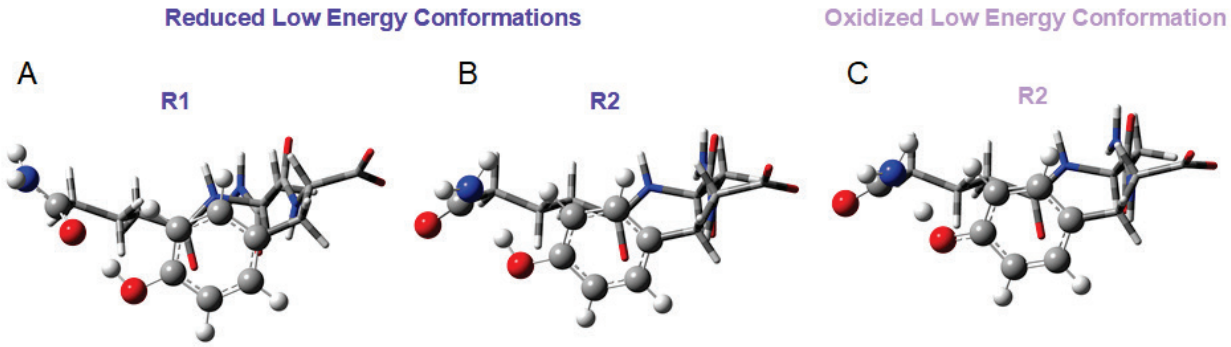

Supplementary Fig. 3. The DFT optimized structures of reduced X1 in the **A**, R1 and **B**, R2 conformation. **c**, Optimized structure of oxidized X1 in the R2 conformation without proton transfer. All structures were optimized in a PCM for water. Although only a small chain is shown, optimizations were performed on the larger Model A structure shown in Supplementary Fig. 2.

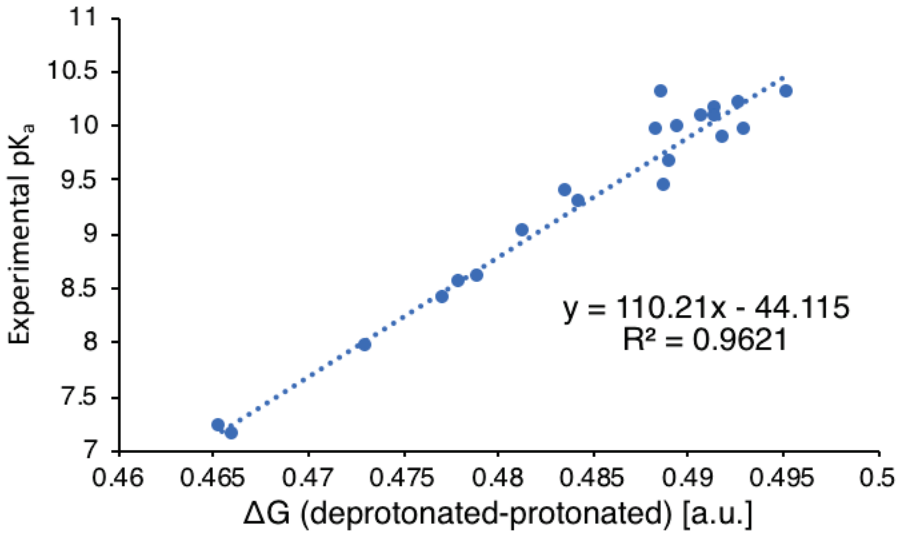

Supplementary Fig. 4. Correlation plot used for calculation of amyloid pK_a values. The DFT-calculated free energy difference between the deprotonated and protonated forms of 21 phenols was correlated with their measured pK_a. The data in this plot is presented in Supplementary Table 2.

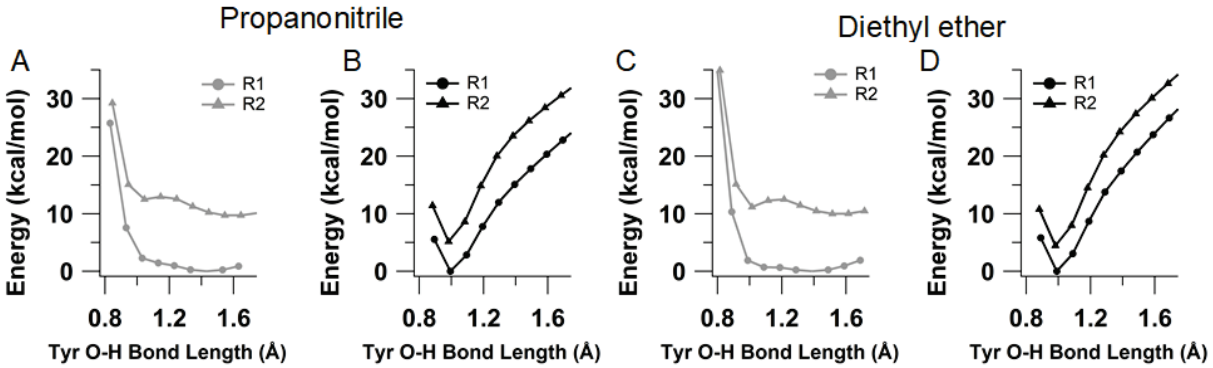

Supplementary Fig. 5. Relaxed potential energy scan for oxidized, **A**, and reduced, **B**, **X1** in R1 and R2 conformations in propanonitrile implicit solvent. Energy is normalized to that of the optimized R1 structures. **C** and **D**, Same calculations as **A** and **B** performed in diethyl ether**.**

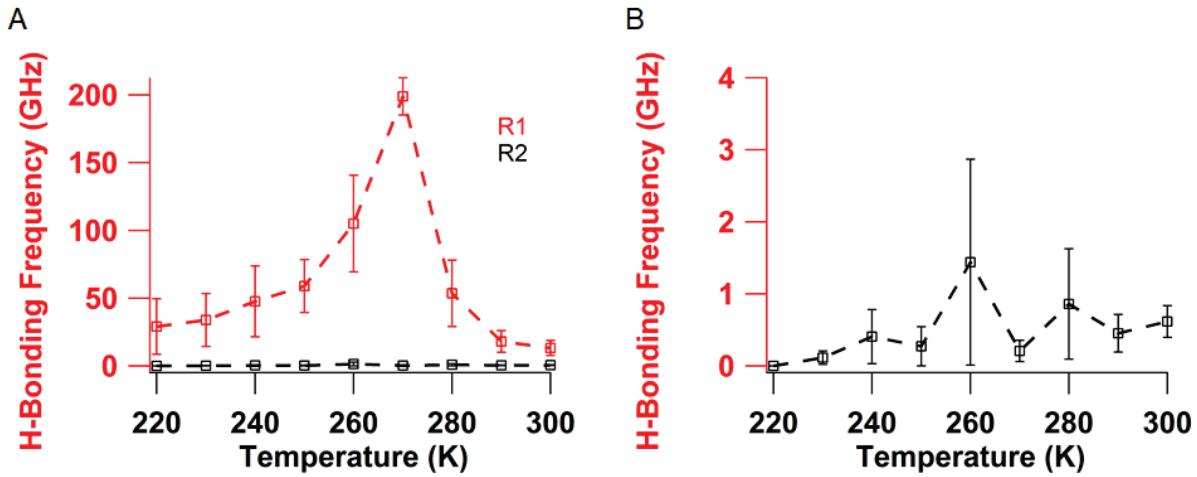

Supplementary Fig. 6. A, Hydrogen bonding frequency comparison between Tyr-O to Gln-O (R1) and Tyr-O to Gln-N (R2) as a function of temperature. **B,** Hydrogen bonding frequency of R2 shown without R1. Error bars represent standard error of the mean.

Supplementary Tables

Supplementary Table 1. Data collection and refinement statistics for KVQIINKL. Statistics for the highest-resolution shell are shown in parentheses.

	KVQIINKL (6NK4)
Wavelength	0.0251
Resolution range	27.24 - 1.994 (2.066 - 1.994)
Space group	P 6_1
Unit cell	62.9 62.9 4.83 90 90 120
Total reflections	5369 (399)
Unique reflections	931 (88)
Multiplicity	5.8 (4.6)
Completeness (%)	96.3 (97.8)
Mean I/sigma(I)	5.53 (1.95)
Wilson B-factor	19.60
R-merge	0.279 (0.7685)
R-meas	0.304 (0.862)
R-pim	0.113 (0.375)
CC1/2	0.981 (0.288)
CC*	0.995 (0.668)
Reflections used in refinement	933 (90)
Reflections used for R-free	84 (10)

R-work	0.278 (0.311)
R-free	0.331 (0.171)
CC(work)	0.761 (0.427)
CC(free)	0.738 (0.572)
Number of non-hydrogen atoms	79
macromolecules	76
solvent	3
Protein residues	9
RMS(bonds)	0.010
RMS(angles)	1.40
Ramachandran favored (%)	100.0
Ramachandran allowed (%)	0.00
Ramachandran outliers (%)	0.00
Rotamer outliers (%)	0.00
Clashscore	0.00
Average B-factor	18.7
macromolecules	18.7
solvent	18.0

Supplementary Table 2. Calculated free energy difference between the protonated and deprotonated forms of 21 phenols with corresponding experimental pK_a values(30).

Molecule	ΔG (deprotonated-protonated) (a.u.)	Experimental pK_a
Phenol	0.489470	9.98
***o*-Methylphenol**	0.488756	10.29
***m*-Methylphenol**	0.490815	10.08
***p*-Methylphenol**	0.491493	10.14
***o*-Chlorophenol**	0.478040	8.56
***m*-Chlorophenol**	0.481374	9.02
***p*-Chlorophenol**	0.483688	9.38
***o*-Nitrophenol**	0.465398	7.23
***m*-Nitrophenol**	0.477206	8.4
***p*-Nitrophenol**	0.466071	7.15
***m*-Cyanophenol**	0.478935	8.61
***p*-Cyanophenol**	0.473129	7.95
***m*-Fluoroophenol**	0.484299	9.28
***p*-Fluorophenol**	0.488438	9.95
***m*-Aminophenol**	0.491956	9.87
***p*-Aminophenol**	0.495299	10.3
***m*-Hydroxyphenol**	0.488762	9.44
***p*-Hydroxyphenol**	0.493004	9.96
***m*-Methoxyphenol**	0.489072	9.65
***p*-Methoxyphenol**	0.492745	10.21
Tyrosine	0.491502	10.07

Supplementary Table 3. DFT-calculated pK_a values of Tyr for X1 model systems with and without Zn^{2+}.

Model	Number of Layers	Zn^{2+} Present	pK_a
A	2	Yes	8.39
B	1	Yes	8.52
C	2	No	7.92
D	1	No	8.50

Supplementary Table 4. Proton transfer distances in optimized X1 structures in three dielectric environments. Propanonitrile and diethyl ether approximate the environments on the surface of and inside proteins respectively. The donor is always the tyrosine oxygen and the acceptors are the glutamine 4 sidechain amide oxygen (R1) or nitrogen (R2). Distances from each of the two energy minima obtained for the oxidized R2 conformation are shown, corresponding to one with a protonated tyrosine and another with a protonated glutamine.

	Donor-Proton Distance (Å)			**Proton-Acceptor Distance (Å)**		
	R1	**R2 (prot. Tyr)**	**R2 (prot. Gln)**	**R1**	**R2 (prot. Tyr)**	**R2 (prot. Gln)**
Water (ε = 78.4)						
Reduced	0.99	0.98	-	1.64	1.93	-
Oxidized	1.44	1.05	1.60	1.05	1.60	1.07
Propanonitrile (ε = 29.3)						
Reduced	0.99	0.98	-	1.64	1.93	-
Oxidized	1.43	1.05	1.60	1.05	1.60	1.07
Diethyl ether (ε = 4.24)						
Reduced	0.99	0.98	-	1.67	1.93	-
Oxidized	1.39	1.01	1.56	1.07	1.71	1.08

Supplementary Table 5. DFT-calculated relative Gibbs free energies of R1 and R2 conformations of reduced X1 in three dielectric environments

Solvent	**G(R2) – G(R1) (kcal/mol)**
Water (ε = 78.4)	+5.3
Propanonitrile (ε = 29.3)	+5.0
Diethylether (ε = 4.24)	+4.4

Supplementary Table 6. DFT-calculated relative Gibbs free energies of R1 and R2 conformations of X1 after oxidation of Tyr. Note that there are two energy minima for the R2 conformation, one in which the Tyr is protonated and one in which Gln is protonated.

Solvent	**Protonated Species in R2**	**G(R2) – G(R1) (kcal/mol)**
Water (ε = 78.4)	Tyr	+13.2
Water (ε = 78.4)	Gln	+11.4
Propanonitrile (ε = 29.3)	Tyr	+13.0
Propanonitrile (ε = 29.3)	Gln	+11.6
Diethylether (ε = 4.24)	Tyr	+12.3
Diethylether (ε = 4.24)	Gln	+12.5

Supplementary Table 7. DFT-calculated oxidation potentials of Tyr for R1 and R2 conformers of X1 in three dielectric environments. SHE conversion from vacuum was 4.44 V (31).

Conformer	**Solvent**	**E_{ox} (V vs SHE)**	**$E_{ox,absolute}$ (V)**
R1	Water (ε = 78.4)	+0.80	+5.24
R1	Propanonitrile (ε = 29.3)	+0.76	+5.20
R1	Diethylether (ε = 4.24)	+0.51	+4.95
R2	Water (ε = 78.4)	+1.14	+5.58
R2	Propanonitrile (ε = 29.3)	+1.11	+5.55
R2	Diethylether (ε = 4.24)	+0.85	+5.29

Supplementary Table 8. DFT-calculated oxidation potentials of Tyr for R1 and R2 conformers of four X1 model systems (described in Supplementary Table 3) in water.

Model	Conformer	E_{ox} (V vs SHE)	$E_{ox,absolute}$ (V)
A	R1	+0.80	+5.24
A	R2	+1.14	+5.58
B	R1	+0.95	+5.39
B	R2	+1.20	+5.64
C	R1	+0.62	+5.06
C	R2	+0.69	+5.13
D	R1	+0.72	+5.16
D	R2	+0.79	+5.23

Supplementary Table 9. Slopes from temperature dependence of conductance form Figure 6a.

	220-260K Slope (Log(S)/K)	260-300K (Log(S)/K)
2-probe	0.0282	-0.0095
4-probe	0.0632	-0.0647

Supplementary Table 10. Table of average resistance, conductivity, and heights for all crystals.

Crystal	Resistance (Ω)	Height (nm)	Conductivity (μS/cm)
X1	2.66E+10 ± 1.05E+10	188 ± 0.28	3.54 ± 0.959
X2	8.51E+11 ± 3.22E+11	76 ± 0.47	0.59 ± 0.199
X3	2.78E+11 ± 8.98E+10	1150 ± 1	0.109 ± 0.0447
X4**	1.56E=12 ± 4.90E+11	74 ± 16	0.347 ± 0.199

Note that ** indicates the 2-probe values reported for resistance and conductivity. Also note that the average value of conductivity is a result of averaging the individual conductivities of all crystals, not the result of using the average values of height and resistance in the conductivity formula.

Supplementary References

1. Rodriguez JA*, et al.* (2015) Structure of the toxic core of α-synuclein from invisible crystals. *Nature* 525:486.
2. Otwinowski Z & Minor W (2001) DENZO and SCALEPACK. *International Tables for Crystallography Volume F: Crystallography of biological macromolecules* ed Rossman MG, Arnold, E. (Springer Netherlands), pp 226-235.
3. McCoy AJ*, et al.* (2007) Phaser crystallographic software. *Journal of Applied Crystallography* 40(4):658-674.
4. Afonine PV*, et al.* (2012) Towards automated crystallographic structure refinement with phenix.refine. *Acta Crystallogr D Biol Crystallogr* 68(Pt 4):352-367.
5. Bricogne G. BE, Brandl M., Flensburg C., Keller P., Paciorek W., & Roversi P SA, Smart O.S., Vonrhein C., Womack T.O. (2016) Buster version 1.10.0 (Global Phasing Ltd., Cambridge, United Kingdom).
6. Murshudov GN*, et al.* (2011) REFMAC5 for the refinement of macromolecular crystal structures. *Acta Crystallographica Section D* 67(4):355-367.
7. Wang F*, et al.* (2019) Structure of Microbial Nanowires Reveals Stacked Hemes that Transport Electrons over Micrometers. *Cell* 177(2):361-369.e310.
8. Tan Y*, et al.* (2016) Synthetic Biological Protein Nanowires with High Conductivity. *Small* 12(33):4481-4485.
9. Kankare J & Kupila E-L (1992) In-situ conductace meausurement during electropolymerization. *Journal Electroanalytical Chemistry* (322):167-181.
10. Becke AD (1993) Density-functional thermochemistry. III. The role of exact exchange. *The Journal of Chemical Physics* 98(7):5648-5652.
11. Lee C, Yang W, & Parr RG (1988) Development of the Colle-Salvetti correlation-energy formula into a functional of the electron density. *Physical Review B* 37(2):785-789.
12. Grimme S, Ehrlich S, & Goerigk L (2011) Effect of the damping function in dispersion corrected density functional theory. *Journal of Computational Chemistry* 32(7):1456-1465.
13. Frisch MJ*, et al.* (2016) Gaussian 16 Rev. C.01Wallingford, CT).
14. Wadt WR & Hay PJ (1985) Ab initio effective core potentials for molecular calculations. Potentials for main group elements Na to Bi. *The Journal of Chemical Physics* 82(1):284-298.
15. Hay PJ & Wadt WR (1985) Ab initio effective core potentials for molecular calculations. Potentials for K to Au including the outermost core orbitals. *The Journal of Chemical Physics* 82(1):299-310.
16. Ditchfield R, Hehre WJ, & Pople JA (1971) Self-Consistent Molecular-Orbital Methods. IX. An Extended Gaussian-Type Basis for Molecular-Orbital Studies of Organic Molecules. *The Journal of Chemical Physics* 54(2):724-728.
17. Hehre WJ, Ditchfield R, & Pople JA (1972) Self—Consistent Molecular Orbital Methods. XII. Further Extensions of Gaussian—Type Basis Sets for Use in Molecular Orbital Studies of Organic Molecules. *The Journal of Chemical Physics* 56(5):2257-2261.
18. Hariharan PC & Pople JA (1973) The influence of polarization functions on molecular orbital hydrogenation energies. *Theoretica chimica acta* 28(3):213-222.

19. Tomasi J, Mennucci B, & Cammi R (2005) Quantum Mechanical Continuum Solvation Models. *Chemical Reviews* 105(8):2999-3094.
20. Dennington R, Keith TA, & Millam JM (2016) GaussView, Version 6 (Semichem Inc., Shawnee Mission, KS).
21. Sawaya MR*, et al.* (2016) Ab initio structure determination from prion nanocrystals at atomic resolution by MicroED. *Proceedings of the National Academy of Sciences, USA* 113(40):11232.
22. Trasatti S (1986) The absolute electrode potential: an explanatory note (Recommendations 1986). in *Pure and Applied Chemistry*, p 955.
23. Li L, Li C, Zhang Z, & Alexov E (2013) On the Dielectric "Constant" of Proteins: Smooth Dielectric Function for Macromolecular Modeling and Its Implementation in DelPhi. *Journal of Chemical Theory and Computation* 9(4):2126-2136.
24. Dudev T, Ilieva S, & Doudeva L (2018) How an electric field can modulate the metal ion selectivity of protein binding sites: insights from DFT/PCM calculations. *Physical Chemistry Chemical Physics* 20(38):24633-24640.
25. Matsui T, Baba T, Kamiya K, & Shigeta Y (2012) An accurate density functional theory based estimation of pKa values of polar residues combined with experimental data: from amino acids to minimal proteins. *Physical Chemistry Chemical Physics* 14(12):4181-4187.
26. Phillips JC*, et al.* (2005) Scalable molecular dynamics with NAMD. *Journal of Computational Chemistry* 26(16):1781-1802.
27. Best RB*, et al.* (2012) Optimization of the Additive CHARMM All-Atom Protein Force Field Targeting Improved Sampling of the Backbone ϕ, ψ and Side-Chain $\chi 1$ and $\chi 2$ Dihedral Angles. *Journal of Chemical Theory and Computation* 8(9):3257-3273.
28. Chen D & Powers L (1995) Synthesis and structures of Zn(C6H12OS2)2(ClO4)2 and Zn(C3H6NS2)2(C3H4N2)— Model compounds for the Zn sites in RNA polymerase. *Journal of Inorganic Biochemistry* 58(4):245-253.
29. Humphrey W, Dalke A, & Schulten K (1996) VMD: Visual molecular dynamics. *Journal of Molecular Graphics* 14(1):33-38.
30. Liptak MD, Gross KC, Seybold PG, Feldgus S, & Shields GC (2002) Absolute pKa Determinations for Substituted Phenols. *Journal of the American Chemical Society* 124(22):6421-6427.
31. McNaught AD & Wilkinson A (1997) IUPAC. Compendium of Chemical Terminology, 2nd ed. (the "Gold Book"). in *Online version (2019-) created by S. J. Chalk* (Blackwell Scientific Publications, Oxford).